



OPEN

SUBJECT AREAS:

SYNTHESIS AND
PROCESSING

NANOWIRES

Received
7 July 2014Accepted
6 October 2014Published
24 October 2014Correspondence and
requests for materials
should be addressed to
W.-R.Y. (woongryu@
snu.ac.kr)* These authors
contributed equally to
this work.

New Electrospinning Nozzle to Reduce Jet Instability and Its Application to Manufacture of Multi-layered Nanofibers

Byoung-Sun Lee^{1,2*}, Seung-Yeol Jeon^{1*}, Haedong Park¹, Geunsung Lee¹, Ho-Sung Yang¹
& Woong-Ryeol Yu¹¹Department of Materials Science and Engineering and Research Institute of Advanced Materials, Seoul National University, 1 Gwanak-ro, Gwanak-gu, Seoul 151-742, Republic of Korea, ²Samsung Advanced Institute of Technology, 130 Samsung-ro, Gyeonggi-do 443-803, Republic of Korea.

A new nozzle system for the efficient production of multi-layered nanofibers through electrospinning is reported. Developed a decade ago, the commonly used coaxial nozzle system consisting of two concentric cylindrical needles has remained unchanged, despite recent advances in multi-layered, multi-functional nanofibers. Here, we demonstrate a core-cut nozzle system, in which the exit pipe of the core nozzle is removed such that the core fluid can form an envelope inside the shell solution. This configuration effectively improves the coaxial electrospinning behavior of two fluids and significantly reduces the jet instability, which was proved by finite element simulation. The proposed electrospinning nozzle system was then used to fabricate bi- and tri-layered carbon nanofibers.

Since the early 1990s, one-dimensional (1-D) nanomaterials have been extensively researched due to their numerous advantages, including minimal structural imperfections per unit volume¹, unusual surface-to-volume ratios²⁻⁴, and excellent material properties⁵. Many studies have been performed on various 1-D forms (*e.g.*, nanoribbons, nanowires, nanorods, and nanofibers) and applied to various fields (*e.g.*, field-effect transistors⁶, imperfect tissue restoration and reconstruction⁷, functional clothing⁸, gas sensors⁹⁻¹¹, filter membranes¹², and energy-storage devices¹³). Recently, 1-D hybridized nanomaterials, such as nanoparticle-encapsulated nanofibers, have demonstrated improved mechanical and electrochemical performance¹⁴⁻¹⁶, as well as amphiphilicity (anti-fouling effect)¹⁷, antimicrobial and ultraviolet protection¹⁸, and controlled drug delivery¹⁹, drawing attention from many researchers and providing new routes for multifunctional material development.

Due to its simple set-up²⁰, mass productivity²¹, size controllability²², and easy composition with other materials²³, electrospinning is one of the most useful processes for fabricating 1-D nanomaterials²⁴⁻²⁶ and hybridizing these materials with multifunctional nanoparticles²⁷⁻²⁹. The main principle of the electrospinning process is the breaking of equilibrium between the surface tension and the electrical force; *i.e.*, charged fluids form a Taylor cone under a strong electric field, from the tip of which the charged jet is ejected when the electrical force overcomes the surface tension²⁴. Various electrospinning studies have been performed for process optimization³⁰ and simulation³¹, characterizations of nanofibers³², energy applications³³, and new process development (*e.g.*, coaxial electrospinning process)³⁴. However, few studies have focused on the new manufacturing processes for multi-layered nanofibers involving multi-coaxial electrospinning, with the exception of core/shell bilayer nanofibers³⁵. This is due mainly to a lack of understanding of multi-coaxial electrospinning, in particular, the fluidic behavior of multi-fluids inside or at the electrospinning nozzle^{34,36-38}.

Since Loscertales *et al.* reported the coaxially electrified jet³⁹, most of the coaxial spinnerets in electrospinning have been designed to have two concentric inner and outer nozzles (Fig. 1(a)). The length of the exit pipe of the core nozzle is equal to that of the outer nozzle; *i.e.*, the core and shell fluids meet at the exit end of the nozzle^{22,40,41}. As a result, two physical phenomena happen almost simultaneously because the junction is located at the end of the outer needle: the shell fluid wraps around the core fluid, while the shell fluid forms a Taylor cone to balance the surface tension and charge accumulation.

Despite the complexity at the nozzle end, few researchers have to our knowledge considered the geometric configuration of the coaxial nozzle in a scientific manner. Thus, this research began with an idea for a new coaxial nozzle, designed to separate the two physical phenomena described above. This novel design was expected to offer

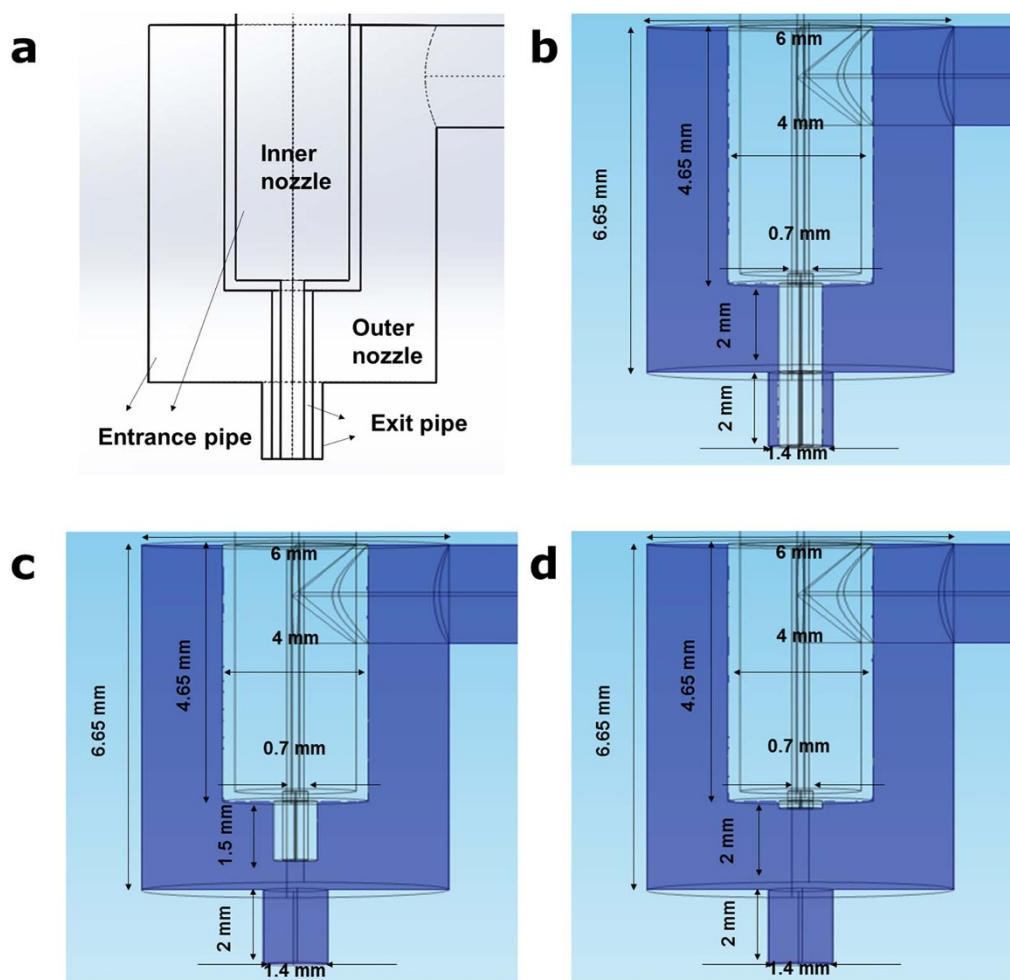


Figure 1 | Schematic diagram of the coaxial nozzle system and the three nozzle systems tested in simulation to investigate the effect of exit pipe length of the core nozzle on the fluidic behavior of the core and shell solutions. (a) General coaxial nozzle and its constitution. (b) Normal nozzle (the exit pipes of the core and shell nozzles meet at the same position). (c) Middle nozzle (the exit pipe length of the core nozzle is shorter than that of the shell nozzle). (d) Core-cut nozzle (the exit pipe of the core nozzle is removed).

more stable coaxial electrospinning conditions, better reproducibility, and facilitate multi-layered nanofiber formation. Note that here ‘stable’ is not related to the whipping phenomenon but to core/shell structure formation.

In this work, the fluidic behaviors of polymer solutions in coaxial nozzles were simulated to investigate the stable condition of the coaxial electrospinning system. Experiments were then performed to confirm the simulation results, in particular, to fabricate multi-layered nanofibers (tri-layered nanofibers) by multi-coaxial electrospinning.

The coaxial electrospinning process was simulated using the finite element method (FEM) and the level set method^{40,41}. Because the simulation capability of the software (COMSOL) was limited to a two-phase flow model, the core and the surrounding environment outside the nozzle were assumed to be air, while a poly(acrylonitrile) (PAN) solution was assumed for the shell material. The liquids were assumed to be incompressible and Newtonian fluids. Furthermore, the immiscibility of the two fluids was assumed. The cylindrical symmetry of the nozzle system created a two-dimensional (2-D) axisymmetric model (Fig. S1). The simulation procedure, including the governing equations, is described in detail in Supplementary Information. The coaxial nozzle system consisted of core and shell nozzles, the pipe length of which could be controlled (Fig. 1(a)). The electrospinning simulation was performed for three nozzle systems having different lengths for the exit pipe of the core nozzle, as follows:

(1) the ‘normal’ nozzle, in which the exit pipes of the core and shell nozzles meet at the same position, (2) the ‘middle’ nozzle, in which the exit pipe of the core nozzle was shortened to half that of the normal nozzle, and (3) the ‘core-cut’ nozzle, in which the exit pipe of the core was removed, as shown in Fig. 1(b)–(d), respectively. The fluidic behavior of the core and shell solutions during coaxial electrospinning was calculated for the three nozzle systems, as shown in Fig. 2 (Movies S2, S3, and S4) in Supplementary Information provide additional information).

Fig. 2 shows that the nanofiber formation occurred in a series of three stages: the envelope formation of the fluid, the thinning of this envelope, and the formation of a Taylor cone. The envelope formation and its thinning, in particular their progression over time, were dependent on the exit-pipe length of the core nozzle. As the exit pipe of the core nozzle was shortened, the growth of the core fluid envelope was delayed by thinning of the core fluid within the exit pipe of the shell nozzle (Fig. 2: a3, b3, and c3). This occurred because the core fluid tried to create an envelope inside the shell fluid, during which the core fluid was stressed by the shear flow of the shell fluid. As a result, in the core-cut nozzle, a high flow rate of the shell fluid was not necessary for Taylor cone formation of the core fluid. Recalling that nanofibers are formed from a jet from the Taylor cone of the fluid, it can be deduced that the core/shell nanofibers can be manufactured more stably in the core-cut nozzle.

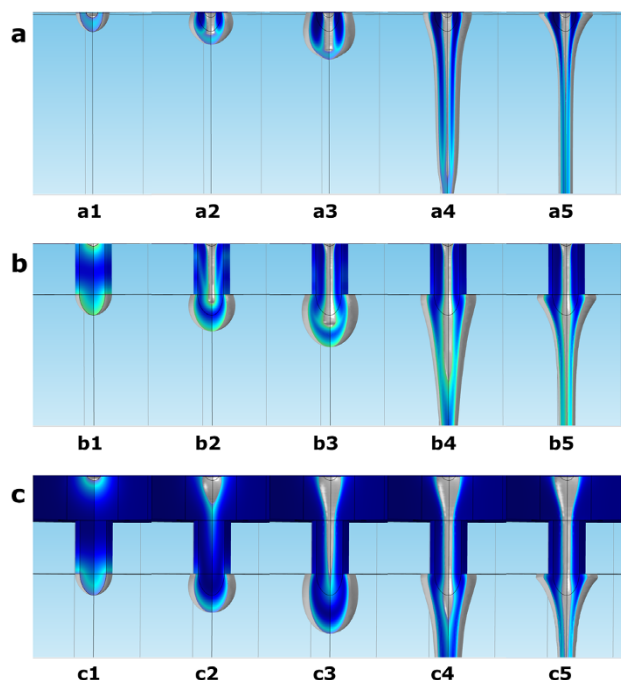


Figure 2 | Simulated spinning behavior of the core and shell fluids during coaxial electrospinning: (a) normal nozzle case, (b) middle nozzle case, and (c) core-cut nozzle case. The numbers (1 through 5) represent the time elapsed after simulation (0, 0.02, 0.05, 0.08, and 0.1 s, respectively). The gray color indicates the interface between the fluids; *i.e.*, the outer and inner gray envelopes represent the interfaces between the poly(acrylonitrile) (PAN) shell solution and the environment (air) outside the shell nozzle, and between the PAN shell and core (air) fluids, respectively. For understanding purposes, the gray envelopes can be thought of as core and shell fluid surfaces. The envelope formation and its thinning behavior, in particular their progression over time, were dependent on the length of the exit pipe of the core nozzle. As the exit pipe of the core nozzle was shortened, the growth of the envelope of the core fluid was delayed by a sharp thinning of the core fluid, making the core fluid thinner within the exit pipe of the shell nozzle.

The instability of the fluid interfaces (between the core and shell, and the shell and the surrounding environment) was evaluated using the simulation results. In the coaxial electrospinning process, the flow instability of fluid was caused by the shear flows at the interface; *e.g.*, two fluids with different shear flow formed an intermediate (mixed) fluid with different potential and kinetic energies from the two fluids. The intermediate fluid expanded over the entire region for the extreme cases; *i.e.*, the two fluids mixed completely. This phenomenon can be explained by Kelvin–Helmholtz (K–H) instabilities^{42,43}. K–H instability was evaluated based on the kinetic and potential energies in parallel shear flows, before and after mixing. This criterion, defined as the Richardson number, states simply that the fluid mixing is stable if the total energy is reduced. The Richardson number is described in detail in the Supplementary Information. Fig. 3 shows the Richardson number distribution over the coaxial electrospinning process; the stable region of the fluid interfaces is indicated by the dark red area, where the Richardson number exceeds 1/4. The shell–environment interface, located ~1 mm away from the entrance of the exit pipe of the shell nozzle tip, was unstable, regardless of the exit-pipe length of the core nozzle. One particularly important finding was that the fluid mixing was stable for core-cut and middle nozzle systems; *i.e.*, a stable fluidic interface was ensured inside the shell nozzle where the core fluid was wrapped by the shell fluid.

The charge distribution within the fluids during coaxial electrospinning was investigated for the three nozzle systems. The transient behavior of the core and shell fluids within the normal nozzle system is shown in Fig. 4, focusing on the charge density distribution, its evolution, and the fluid front formation during coaxial electrospinning. As time progressed, the charge eventually migrated to the shell–environment interface; this is indicated in Fig. 4(c) by the light yellow color. The charged fluid then moved under the effect of external electrical forces. Finally, the shell–air interface shrank in the normal direction and stretched along the tangential direction (Fig. 4(c)–(h)), because the electrical displacement was discontinuous with respect to the interface normal direction and the charged fluid was dragged to the ground continuously^{44,45}. As thinning of the fluid occurred, the charge near the nozzle end became more concentrated. Under these conditions, minimal charge accumulation occurred at the interface between the core and shell fluids; thus, the core fluid was dragged by the shear flow of the shell fluids (we will investigate this in more detail later). In summary, due to charge conduction, the migrating charges first became concentrated at the shell–environment interface, particularly at the tip of the envelope and around the nozzle end. As the fluid was dragged and thinned by the external electrical force, the charges moved by convection. As a result, charges accumulated along the shell–environment interface. Here, we observed two phenomena: (1) an unexpected flow front and (2) the formation of surface charge on the core fluid (Fig. 4(c)–(h), indicated by the light blue color) and at the corner point of the nozzle end. The flow front of the shell fluid became wider beyond the shell nozzle and expanded further, as shown in Fig. 4(b)–(h). This behavior was attributed to the boundary conditions. The wall condition was imposed on the horizontal line near the nozzle end, such that the shell fluid moved along the boundary (Fig. S3). In reality, such a boundary condition does not exist, which may contribute to the formation of a small, sharp Taylor cone. In the current simulation, our main focus was to investigate the effect of the three nozzle systems on the spinning behavior; thus, the wall boundary condition was imposed to reduce the computation domain and computation time. The charges on the surface of the core fluid and at the edge between the shell and the surrounding wall were bound charges due to polarization, the effect of which is discussed below in detail.

The distribution of space charge was compared for the three nozzle systems, as shown in Fig. 5. The charge on the surface of the core fluid disappeared as the exit pipe of the core nozzle was shortened. Because free charge migrated to the shell–environment interface, the charge observed on the surface of the core fluid (*i.e.*, the interface between the core and shell fluids) was attributed to polarization bound charges. This bound charge induced the formation of a free-charge concentration around the shell fluid. The concentration of free charges was particularly noticeable on the upper part of the stream, in that the maximum charge of the normal nozzle system (0.8596 C m^{-3}) was larger than that of the middle (0.2423 C m^{-3}) and core-cut (0.2485 C m^{-3}) nozzle systems. Polarized bound charge also accumulated near the edge of the exit pipe; however, its concentration was highest for the normal nozzle system (Fig. 6). As a result, equipotential surfaces were set up inside the nozzle; a discontinuous potential distribution was observed outside the nozzle. This discontinuity induced high polarization in the core and shell fluids, which affected the electrical forces. The polarization effect was strongest for the normal nozzle system, because the exit pipe of the inner nozzle underwent a potential discontinuity compared with the other two cases. This high polarization may produce unnecessary electrical forces acting on the core–shell and shell–environment interfaces (Fig. S5, Supplementary Information). Excessive electrical force (for creating the jet) may induce jet instabilities. Simulation results indicated that the electrical force for jet formation was minimal for the core-cut nozzle system, implying that the core-cut nozzle design was, indeed, beneficial with regard to reducing jet instability.

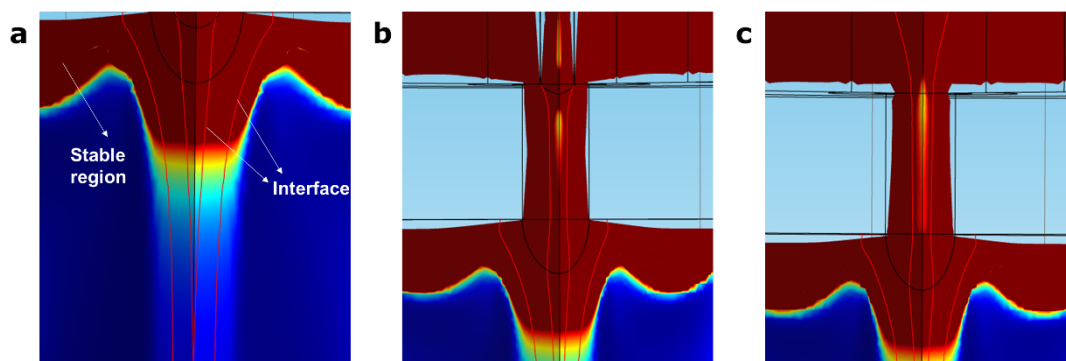


Figure 3 | Kelvin-Helmholtz (K-H) instability as a function of the Richardson number distributed over fluids in Fig. 2 a5), b5), and c5): (a) normal nozzle, (b) middle nozzle, and (c) core-cut nozzle. The red lines represent the core-shell interface and shell-air interface. The dark red area represents the fluid sections, in which the Richardson number exceeds 1/4, (stable area by K-H instability criterion).

Finally, the velocity profiles of the core and shell fluids were investigated, focusing on the intersection of the core and shell fluids (Fig. 7). Because the nozzle was cylindrical in shape, laminar pipe flow with a parabolic velocity profile was observed. As the diameter of the pipe decreased, a steeper velocity profile was observed. For the normal and middle nozzles, the velocity profile of the core fluid changed considerably when the core fluid met the shell fluid (Fig. 7(a) and (b)). However, the shell fluid in the core-cut nozzle did not pass the narrow pipe-like region therefore, the velocity profile remained smooth. Accordingly, the core fluid flowed stably inside the shell fluid, without distinct deformation of the velocity profile. Thus, these results indicated that the core-cut nozzle configuration was the most advantageous of the three nozzle types with regard to stable formation of the core-shell interface and multi-layered nanofibers.

The new findings from the electrospinning simulation of the core-cut nozzle were validated experimentally. SAN-core/PAN-shell nanofibers were electrospun and thermally treated to produce hollow carbon nanofibers (HCNFs)^{46–48}. Here, the concentrations of the PAN and SAN solutions in DMF were 20 and 30 wt%, respectively. The coaxial electrospinning conditions were set: the flow rate of the PAN shell solution was 1.00 mL h⁻¹, the applied voltage was 18 kV, and the tip-to-collector distance was 15 cm. We used two flow rates for the SAN core solution: 0.50 and 1.00 mL h⁻¹. The former was selected to investigate the morphologies of the core/shell structures according to different nozzle systems used in the simulation, while the latter was to show the limitation of the normal nozzle.

As shown in Fig. 8 (a)–(c), the hollow structure of the prepared nanofibers was successfully formed from all of the three nozzle systems. The typical cross-sectional shapes of nanofibers were, however, quite different from each other. The cross-sections of the HCNFs prepared using the normal and middle nozzles were highly elliptic (in both outer and inner circumference). In contrast, the HCNFs prepared using the core-cut nozzle showed more circular outer and inner circumferences (for quantitative comparison, we measured the eccentricities of the outer and inner circumferences as listed in Table S3). Note that the closer the eccentricity value is to zero, the more circular the ellipse^{48,49}. Furthermore, the hole of HCNFs was more coaxially formed in the HCNFs manufactured using the core-cut nozzle. We believe that more desirable cross-sectional shape of HCNFs manufactured from the core-cut nozzle was attributed to the fact that the core solution envelope was sufficiently guided by the shell solution in the core-cut nozzle, while the core solution envelopes of the normal and middle nozzles experienced the abrupt change of the velocity and subsequent thinning behavior (as shown in Fig. 7). As the flow rate of the SAN core solution increased to 1.00 mL h⁻¹, we observed that the hollow structure was not formed in the nanofibers prepared using the normal nozzle, i.e., the core solution was not perfectly covered by the shell solution (Fig. 8(d)). The HCNFs prepared using the core-cut and middle nozzles showed uniform hollow structures (Fig. 8(e) and (f)). Therefore, it can be concluded that the core-cut nozzle is more beneficial to produce better-developed core/shell nanofibers.

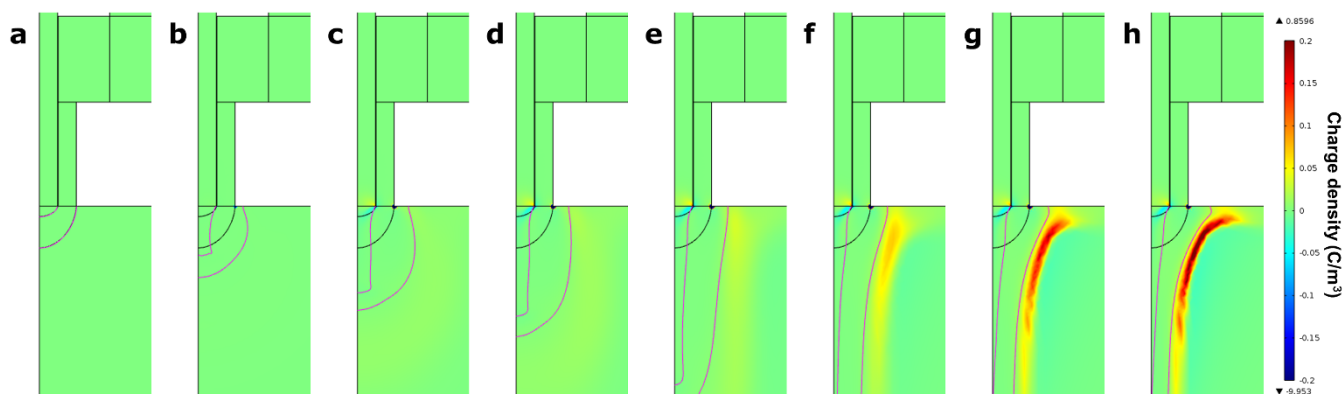


Figure 4 | Transient behavior of the core and shell fluids at (a) 0, (b) 0.02, (c) 0.05, (d) 0.06, (e) 0.07, (f) 0.08, (g) 0.09, and (h) 0.1 s after application of the electric field. The space charge distribution is shown as a color contour map, while the flow fronts of the fluids and their evolution are described by red lines.

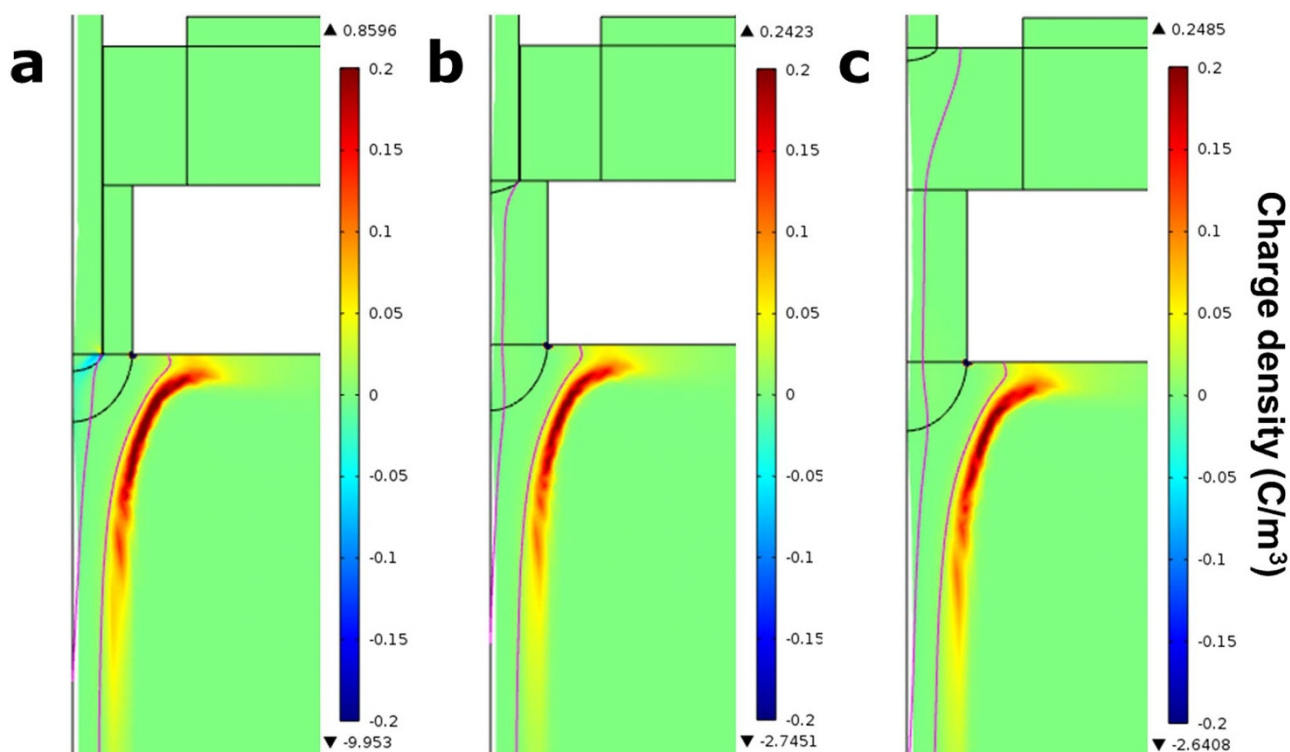


Figure 5 | Space charge distribution of the core and shell fluids at 0.1 s during coaxial electrospinning: (a) normal nozzle case, (b) middle nozzle case, and (c) core-cut nozzle case. The purple lines represent the core–shell and shell–environment interfaces.

The core-cut nozzle was then retrieved to control the hollowness and wall thickness of the HCNFs. Note that the hollowness and wall thickness were successfully controlled using a general coaxial nozzle and controlling several of the processing parameters (*i.e.*, the SAN flow rate, SAN concentration, and PAN concentration)⁴⁸. The flow rates of the PAN solution, however, could not be reduced beyond 1.00 mL h⁻¹. A lower flow rate for the PAN solution would provide an efficient means of producing thinner HCNFs; however, these lower rates tended to produce C-shaped CNFs instead of hollow CNFs, due to the insufficient volume of the shell solution wrapping the core. The flow rate of the PAN solution could be lowered when the core-cut nozzle was used, which was probably due to the thinning of the core fluid inside the shell nozzle. Fig. 9(a)–(c) show field-

emission scanning electron microscopy (FE-SEM) images of the morphological change of the resulting HCNFs, according to the flow rate of the PAN solution, for a constant SAN flow rate of 0.50 mL h⁻¹. The wall of the HCNFs fabricated with the low flow rate of the PAN shell solution (0.25 mL h⁻¹) was wrinkled, but became more circular as the flow rate of the PAN solution increased. Fig. 9(d)–(f) show the morphologies of the HCNFs fabricated using various PAN flow rates for a fixed SAN flow rate of 0.25 mL h⁻¹. The reduced core rate brought about the circular shape of the HCNFs without wrinkling, and also reduced the wall thickness (Fig. 9(g)). One interesting observation was the slight change in the outer diameter of the HCNFs (*e.g.*, from 578 (±76) to 609 (±108) nm) as the flow rate of the PAN solution increased; whereas the inner diameter of the HCNFs

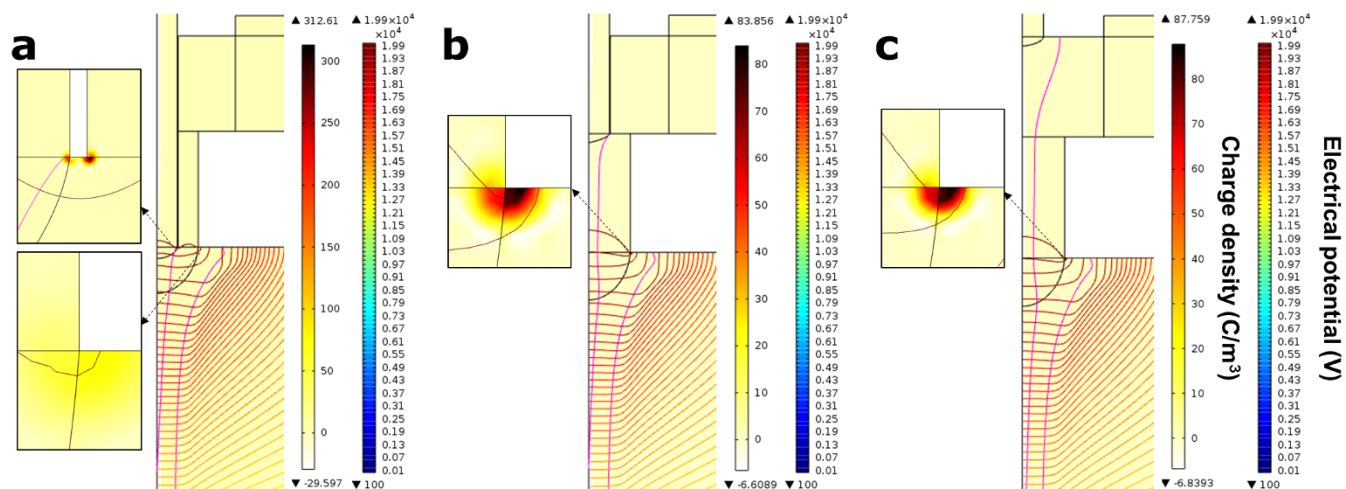


Figure 6 | Polarization charge density and isocontours of potential at 0.1 s. (a) Normal nozzle case. (b) Middle nozzle case. (c) Core-cut nozzle case. The purple lines represent the core/shell interface and shell/air interface.

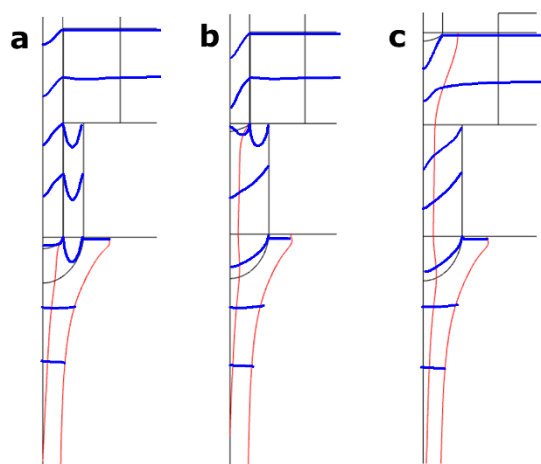


Figure 7 | Velocity profiles of core-shell fluids during coaxial electrospinning at 0.1 s: (a) normal nozzle case, (b) middle nozzle case, and (c) core-cut nozzle case. The red lines represent the core-shell and shell-air interfaces. The blue lines represent the velocity profile near the intersection of the core and shell fluids.

decreased notably from 425 (± 77) to 327 (± 74) nm, implying that the increased shell volume resulted in greater elongation of the core solution by shear dragging.

Multi-layered nanofibers were manufactured using triple coaxial electrospinning and the core-cut nozzle. A tri-layered core-cut nozzle (Fig. S1(e)) was designed to make stable envelopes of the core and medium fluids within the shell fluids, respectively. The processing parameters used are listed in Table 1. Concentrically tri-layered, PAN-core/SAN-medium/PAN-shell nanofibers were electrospun using the core-cut nozzle. First, the internal structure of the as-spun tri-layered nanofibers was examined using transmission electron microscopy (TEM). Although a slight contrast difference was observed (Fig. 10(a)), no significant interfaces between the layers were evident. To observe the boundaries between adjacent layers, the SAN in the middle layer was selectively dissolved using acetone;

a wire-in-tube shape in the selectively dissolved tri-layered nanofiber was observed, clearly demonstrating the successful formation of tri-layered nanofibers (Fig. 10(b)). Fig. 10(c) shows the CNFs in a wire-in-tube structure, after thermal treatment (stabilization and carbonization). The multi-layered CNF tubes were circular in shape, while the wire inside the tube was elliptical. This was probably due to insufficient shear dragging of the medium fluids. Porous wire-in-solid tube-structured nanofibers were also manufactured, as shown in Fig. 10(d). The porous wire was prepared simply by introducing the core solution to a SAN/PAN emulsion (SAN: PAN = 1:3, 20 wt%)⁴⁹. Circular pores formed as a result of thermal degradation of the SAN islands within the PAN matrix. Finally, a porosity gradient structure was obtained by changing the core and medium solutions using SAN/PAN emulsions (Fig. 10(e)). The larger pores in the core were surrounded by small pores (<100 nm). The SAN contents of the core and medium solutions were 50 and 25 wt%, respectively. Despite the presence of the pores at the core and in the middle layer, the skin shell of the CNFs was solid (having been converted from the PAN shell). Various structures in the multi-layered nanofibers could be generated using the core-cut nozzle, despite significant changes in the solution properties, such as the viscosity and conductivity. This showed that the core-cut nozzle system was highly suitable for manufacturing multi-layered nanofibers using electrospinning.

In summary, the suitability of a core-cut nozzle system in the electrospinning process for manufacturing stable multi-layered nanofibers was demonstrated numerically and experimentally. The envelope of the core solution formed inside the shell fluid in the core-cut nozzle, enabling control over the wall thickness and hollowness of the multi-layered nanofibers. Using a tri-layered core-cut nozzle, concentrically tri-layered nanofibers (PAN-core/SAN-medium/PAN-shell) were successfully manufactured, demonstrating the potential of the core-cut nozzle system for manufacturing multi-layered nanofibers with various structures.

Methods

Numerical simulations. To simulate the coaxial electrospinning process, three governing equations were coupled to each other. To reduce the computation time, the simulation was confined to nozzles with an axisymmetric geometry. Liquids were

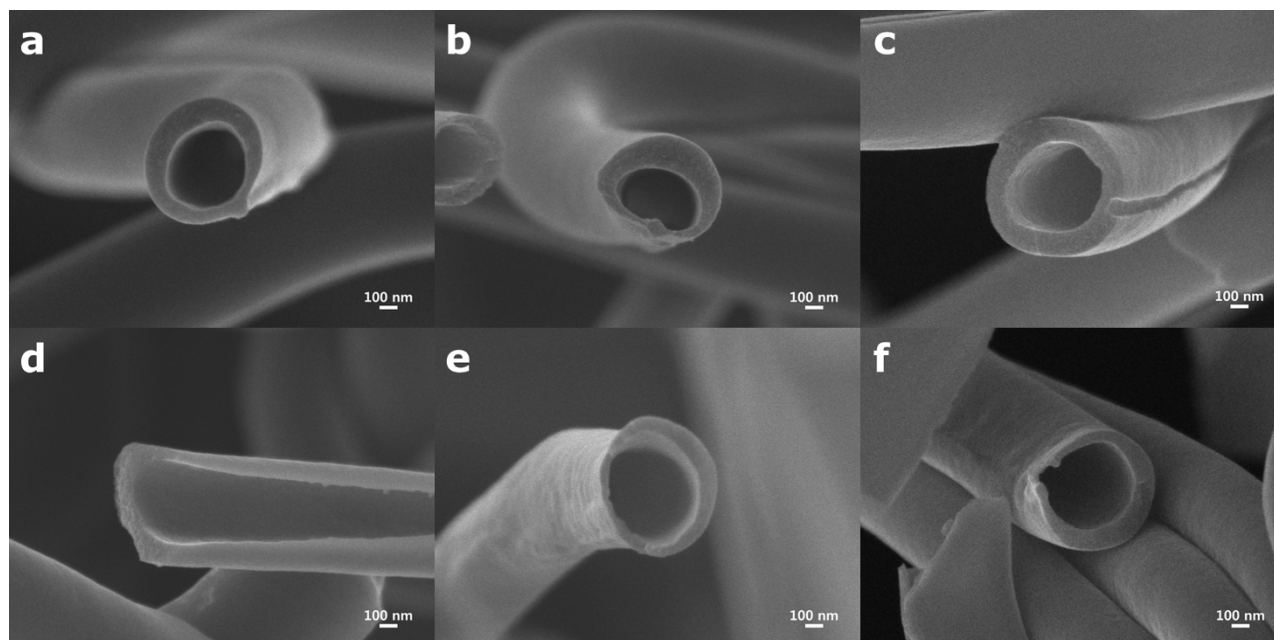


Figure 8 | The morphologies of hollow carbon nanofibers manufactured using different nozzle systems, (a) normal nozzle, (b) middle nozzle, and (c) core-cut nozzle, with the flow rate of the SAN core solution of 0.50 mL h⁻¹. (d), (e), and (f) represent the morphologies of hollow carbon nanofibers manufactured using the three nozzle systems with different flow rate of the SAN solution (1.00 mL h⁻¹).

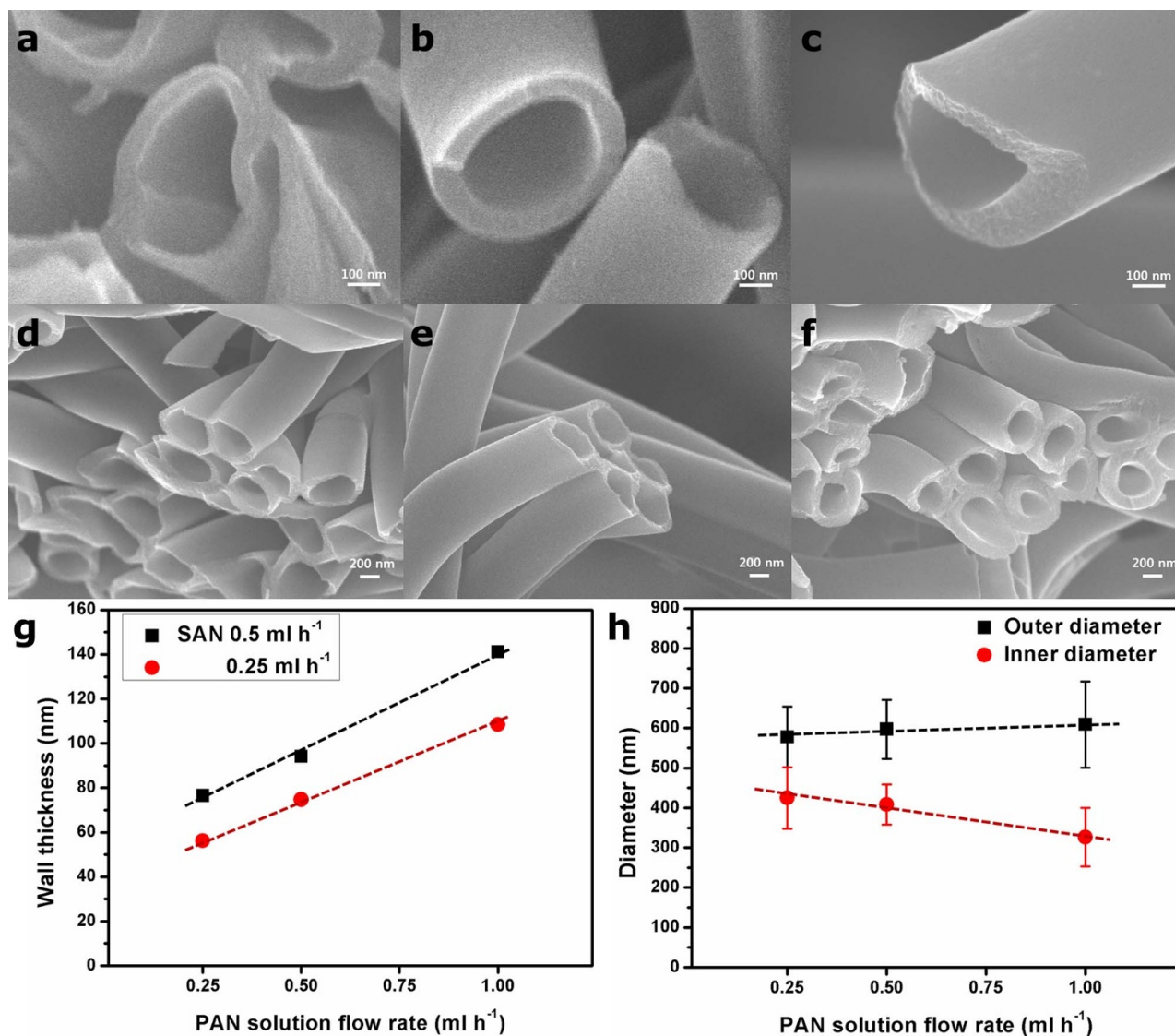


Figure 9 | Field-emission scanning electron microscopy (FE-SEM) images of the hollow carbon nanofibers (HCNFs) fabricated by coaxial electrospinning of styrene-co-acrylonitrile (SAN)/PAN solutions using the core-cut nozzle and subsequent thermal treatment. The flow rate of the PAN (shell) solution changed from 0.25 to 0.50 and 1.00 mL h⁻¹, while the flow rate of the SAN (core) solution was (a–c) 0.50 mL h⁻¹ and (d–f) 0.25 mL h⁻¹. (g) Wall thickness change and (h) the inner and outer diameter of the HCNFs according to the flow rate of the PAN shell solution. The flow rate of the SAN solution was 0.25 mL h⁻¹ for (h).

assumed to be incompressible and Newtonian fluids. Note that frequently the non-Newtonian fluids in many electrospinning simulation studies were simplified as Newtonian ones by disregarding the elastic effects due to drying of the jet and the simulation results were very well matched with the experimental results^{45,50}. Thus, the Navier–Stokes equation was used to describe the motion of the interfaces between the core and shell fluids and between the shell fluid and the surrounding air, and solved using the level set equation. The details were described in Supplementary Information.

Preparation of hollow carbon nanofiber using a core-cut nozzle. Bi- and tri-layered nanofibers were fabricated using a novel nozzle system, which was designed based on the simulation results (see Fig. S1). Poly (acrylonitrile) (PAN, M_w : 200,000 g mol⁻¹, Misui Chemical) and styrene-co-acrylonitrile (SAN, M_w : 120,000 g mol⁻¹, AN = 28.5 mol%, Cheil Industries) were used as the carbonizing precursor and thermally degradable polymer, respectively. PAN and SAN were dissolved in *N,N*-dimethylformamide (DMF, 99.5%), where the concentrations of PAN and SAN were 20 wt% and 30 wt%, respectively. Note that PAN and SAN solutions were

Table 1 | Summary of standard tri-layered coaxial electrospinning conditions

Parameters	Core	Medium	Shell
Composition	PAN 20 wt%	SAN 30 wt%	PAN 20 wt%
Flow rate	0.25 mL h ⁻¹	0.50 mL h ⁻¹	0.75 mL h ⁻¹
Applied voltage		18 kV	
TCD		15 cm	

PAN: poly(acrylonitrile); SAN: styrene-co-acrylonitrile; TCD: tip-to-collector distance.

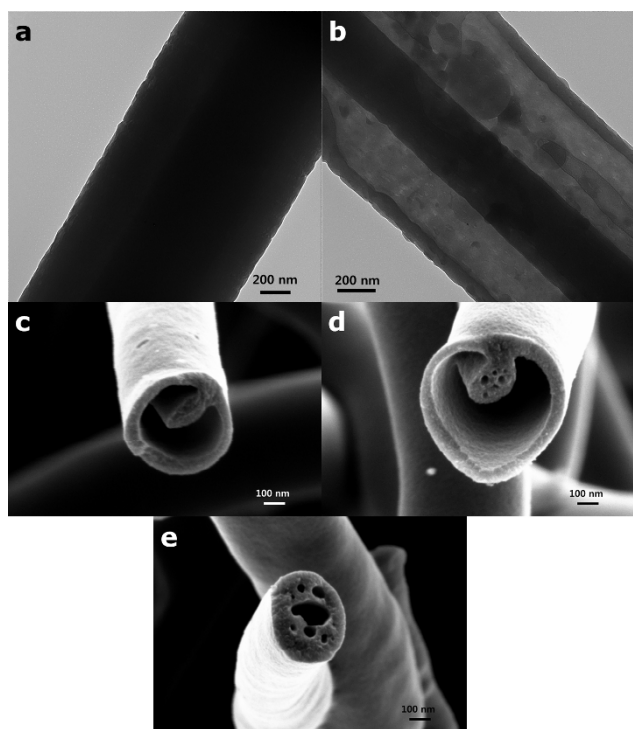


Figure 10 | Tri-layered nanofibers prepared using a tri-layered core-cut nozzle. Transmission electron microscopy (TEM) images of (a) an as-spun PAN-core/SAN-medium/PAN-shell nanofiber, and (b) a SAN selectively dissolved PAN-core/SAN-medium/PAN-shell nanofiber, (c) wire-in-tube shaped CNFs, (d) porous wire-in-solid tube-shaped CNFs, and (e) the porosity gradient of the CNFs.

phenomenologically proved to be immiscible (see supplementary information)¹⁸. The applied voltage was 18 kV, and the tip-to-collector distance was 15 cm. The coaxially electrospun nanofibers were thermally treated for oxidative stabilization (at 270–300°C for 1 h in air atmosphere) and carbonization (at 1000°C for 1 h in an N₂ atmosphere) of the PAN layer. The rate of temperature increase was set at 10°C min⁻¹.

- Hwang, K. Y., Kim, S.-D., Kim, Y.-W. & Yu, W.-R. Mechanical characterization of nanofibers using a nanomanipulator and atomic force microscope cantilever in a scanning electron microscope. *Polym. Test* **29**, 375–380 (2010).
- Wang, X. *et al.* Electrospun Nanofibrous Membranes for Highly Sensitive Optical Sensors. *Nano Lett.* **2**, 1273–1275 (2002).
- Wnek, G. E., Carr, M. E., Simpson, D. G. & Bowlin, G. L. Electrospinning of Nanofiber Fibrinogen Structures. *Nano Lett.* **3**, 213–216 (2002).
- Kim, I.-D. *et al.* Ultrasensitive Chemiresistors Based on Electrospun TiO₂ Nanofibers. *Nano Lett.* **6**, 2009–2013 (2006).
- Arshad, S. N., Naraghi, M. & Chasiotis, I. Strong carbon nanofibers from electrospun polyacrylonitrile. *Carbon* **49**, 1710–1719 (2011).
- Li, Y., Qian, F., Xiang, J. & Lieber, C. M. Nanowire electronic and optoelectronic devices. *Mater. Today* **9**, 18–27 (2006).
- Pham, Q. P., Sharma, U. & Mikos, A. G. Electrospinning of polymeric nanofibers for tissue engineering applications: a review. *Tissue Eng.* **12**, 1197–1211 (2006).
- Lee, S. & Obendorf, S. K. Use of Electrospun Nanofiber Web for Protective Textile Materials as Barriers to Liquid Penetration. *Text. Res. J.* **77**, 696–702 (2007).
- Kim, W.-S. *et al.* SnO₂ nanotubes fabricated using electrospinning and atomic layer deposition and their gas sensing performance. *Nanotechnology* **21**, 245605 (2010).
- Cho, S. *et al.* Ethanol sensors based on ZnO nanotubes with controllable wall thickness via atomic layer deposition, an O₂ plasma process and an annealing process. *Sensor Actuat. B: Chem.* **162**, 300–306 (2012).
- Lee, B.-S. *et al.* Fabrication of SnO₂ nanotube microyarn and its gas sensing behavior. *Smart Mater. Struct.* **20**, 105019 (2011).
- Ma, Z., Kotaki, M. & Ramakrishna, S. Electrospun cellulose nanofiber as affinity membrane. *J. Membr. Sci.* **265**, 115–123 (2005).
- Chan, C. K. *et al.* High-performance lithium battery anodes using silicon nanowires. *Nat. Nanotechnol.* **3**, 31–35 (2008).
- Lee, B.-S. *et al.* Novel multi-layered 1-D nanostructure exhibiting the theoretical capacity of silicon for a super-enhanced lithium-ion battery. *Nanoscale* **6**, 5989–5998 (2014).

- Lee, B.-S. *et al.* Facile conductive bridges formed between silicon nanoparticles inside hollow carbon nanofibers. *Nanoscale* **5**, 4790–4796 (2013).
- Lee, B.-S. *et al.* Fabrication of Si core/C shell nanofibers and their electrochemical performances as a lithium-ion battery anode. *J. Power Sources* **206**, 267–273 (2012).
- Cho, Y. *et al.* Preparation and Characterization of Amphiphilic Triblock Terpolymer-Based Nanofibers as Antifouling Biomaterials. *Biomacromolecules* **13**, 1606–1614 (2012).
- Pant, H. R. *et al.* Electrospun nylon-6 spider-net like nanofiber mat containing TiO₂ nanoparticles: A multifunctional nanocomposite textile material. *J. Hazard. Mater.* **185**, 124–130 (2011).
- Wang, C., Yan, K.-W., Lin, Y.-D. & Hsieh, P. C. H. Biodegradable Core/Shell Fibers by Coaxial Electrospinning: Processing, Fiber Characterization, and Its Application in Sustained Drug Release. *Macromolecules* **43**, 6389–6397 (2010).
- Ramakrishna, S. *et al.* Electrospun nanofibers: solving global issues. *Mater. Today* **9**, 40–50 (2006).
- Ahn, S., Lee, H., Park, G.-M. & Kim, G. Fabrication of poly(methyl methacrylate) micro-droplets using a complex electric field on a rolling collector. *Macromol. Res.* **18**, 429–434 (2010).
- Li, D. & Xia, Y. Direct Fabrication of Composite and Ceramic Hollow Nanofibers by Electrospinning. *Nano Lett.* **4**, 933–938 (2004).
- Huang, Z.-M., Zhang, Y. Z., Kotaki, M. & Ramakrishna, S. A review on polymer nanofibers by electrospinning and their applications in nanocomposites. *Compos. Sci. Technol.* **63**, 2223–2253 (2003).
- Doshi, J. & Reneker, D. H. Electrospinning process and applications of electrospun fibers. *J. Electrostat.* **35**, 151–160 (1995).
- Li, D. & Xia, Y. Electrospinning of Nanofibers: Reinventing the Wheel? *Adv. Mater.* **16**, 1151–1170 (2004).
- Reneker, D. H. & Chun, I. Nanometre diameter fibres of polymer, produced by electrospinning. *Nanotechnology* **7**, 216 (1996).
- Mavis, B. A strategy for biomimetic hybridization of electrospun fiber mat cross-sections. *Mater. Sci. Eng. C* **31**, 1357–1362 (2011).
- Song, J.-H., Yoon, B.-H., Kim, H.-E. & Kim, H.-W. Bioactive and degradable hybridized nanofibers of gelatin-siloxane for bone regeneration. *J. Biomed. Mater. Res. A* **84A**, 875–884 (2008).
- Sui, X. M., Shao, C. L. & Liu, Y. C. White-light emission of polyvinyl alcohol/ZnO hybrid nanofibers prepared by electrospinning. *Appl. Phys. Lett.* **87**, 113115 (2005).
- Deitzel, J. M., Kleinmeyer, J., Harris, D. & Beck Tan, N. C. The effect of processing variables on the morphology of electrospun nanofibers and textiles. *Polymer* **42**, 261–272 (2001).
- Lu, C., Chen, P., Li, J. & Zhang, Y. Computer simulation of electrospinning. Part I. Effect of solvent in electrospinning. *Polymer* **47**, 915–921 (2006).
- Naraghi, M., Ozkan, T., Chasiotis, I., Hazra, S. S. & Boer, M. P. d. MEMS platform for on-chip nanomechanical experiments with strong and highly ductile nanofibers. *J. Micromech. Microeng.* **20**, 125022 (2010).
- Ji, L. & Zhang, X. Fabrication of porous carbon nanofibers and their application as anode materials for rechargeable lithium-ion batteries. *Nanotechnology* **20**, 155705 (2009).
- Chen, H. *et al.* Nanowire-in-Microtube Structured Core/Shell Fibers via Multifluidic Coaxial Electrospinning. *Langmuir* **26**, 11291–11296 (2010).
- Zhang, J.-F. *et al.* Electrospun Core-Shell Structure Nanofibers from Homogeneous Solution of Poly(ethylene oxide)/Chitosan. *Macromolecules* **42**, 5278–5284 (2009).
- Kalra, V., Lee, J. H., Park, J. H., Marquez, M. & Joo, Y. L. Confined Assembly of Asymmetric Block-Copolymer Nanofibers via Multiaxial Jet Electrospinning. *Small* **5**, 2323–2332 (2009).
- Ahmad, Z. *et al.* Generation of multilayered structures for biomedical applications using a novel tri-needle coaxial device and electrohydrodynamic flow. *J. R. Soc. Interface* **5**, 1255–1261 (2008).
- Han, D. & Steckl, A. J. Triaxial Electrospun Nanofiber Membranes for Controlled Dual Release of Functional Molecules. *ACS Appl. Mater. Interfaces*, (2013).
- Loscertales, I. G. *et al.* Micro/Nano Encapsulation via Electrified Coaxial Liquid Jets. *Science* **295**, 1695–1698 (2002).
- Yue, P., Feng, J. J., Liu, C. & Shen, J. A diffuse-interface method for simulating two-phase flows of complex fluids. *J. Fluid Mech.* **515**, 293–317 (2004).
- Olsson, E. & Kreiss, G. A conservative level set method for two phase flow. *J. Comput. Phys.* **210**, 225–246 (2005).
- Miles, J. W. On the generation of surface waves by shear flows Part 3. Kelvin-Helmholtz instability. *J. Fluid Mech.* **6**, 583–598 (1959).
- Van Dyke, M. *Perturbation methods in fluid mechanics.* (Academic Press, 1964).
- Yu, D.-G. *et al.* Linear drug release membrane prepared by a modified coaxial electrospinning process. *J. Membr. Sci.* **428**, 150–156 (2013).
- Yan, F., Farouk, B. & Ko, F. Numerical modeling of an electrostatically driven liquid meniscus in the cone-jet mode. *J. Aerosol Sci.* **34**, 99–116 (2003).
- Lee, B.-S. *et al.* Face-Centered-Cubic Lithium Crystals Formed in Mesopores of Carbon Nanofiber Electrodes. *ACS Nano* **7**, 5801–5807 (2013).
- Lee, B.-S. *et al.* Anodic properties of hollow carbon nanofibers for Li-ion battery. *J. Power Sources* **199**, 53–60 (2012).
- Lee, B.-S., Park, K.-M., Yu, W.-R. & Youk, J. An effective method for manufacturing hollow carbon nanofibers and microstructural analysis. *Macromol. Res.* **20**, 605–613 (2012).



49. Lee, B.-S. *et al.* Effect of Pores in Hollow Carbon Nanofibers on Their Negative Electrode Properties for a Lithium Rechargeable Battery. *ACS Applied Materials & Interfaces* **4**, 6702–6710 (2012).
50. Lim, L. K., Hua, J., Wang, C.-H. & Smith, K. A. Numerical simulation of cone-jet formation in electrohydrodynamic atomization. *AIChE J.* **57**, 57–78 (2011).

Acknowledgments

This research was supported by Mid-career Researcher Program through NRF grant funded by the MSIP (2013R1A2A2A01067717).

Author contributions

B.L. and W.Y. designed the concept and experiments. B.L., G.L. and H.Y. performed the experiments. S.J. and H.P. analyzed the fluidic behavior with the COMSOL software. B.L., S.J. and W.Y. co-wrote the paper. W.Y. conceived and guided the project. All authors discussed the results and commented on the manuscript at all stages.

Additional information

Supplementary information accompanies this paper at <http://www.nature.com/scientificreports>

Competing financial interests: The authors declare no competing financial interests.

How to cite this article: Lee, B.-S. *et al.* New Electrospinning Nozzle to Reduce Jet Instability and Its Application to Manufacture of Multi-layered Nanofibers. *Sci. Rep.* **4**, 6758; DOI:10.1038/srep06758 (2014).



This work is licensed under a Creative Commons Attribution-NonCommercial-NoDerivs 4.0 International License. The images or other third party material in this article are included in the article's Creative Commons license, unless indicated otherwise in the credit line; if the material is not included under the Creative Commons license, users will need to obtain permission from the license holder in order to reproduce the material. To view a copy of this license, visit <http://creativecommons.org/licenses/by-nc-nd/4.0/>